Optically Transparent Metasurface Radome for RCS Reduction and Gain Enhancement of Multifunctional Antennas

Trung D. Ha, *Graduate Student Member, IEEE*, Liang Zhu, *Student Member, IEEE*, Nabeel AlSaab, Pai-Yen Chen, *Senior Member, IEEE*, and Jay L. Guo

***Abstract*— In this article, we theoretically propose and experimentally demonstrate a compact, optically transparent metasurface radome with asymmetric electromagnetic absorption for making low-radar cross section (RCS) and gain-enhanced multifunctional antennas. The proposed unseeable metasurface has a bilayer structure consisting of periodically patterned and unpatterned transparent conductive films separated by a thin acrylic layer. Such a bilayer metasurface is highly reflective when illuminated by microwave from one side, while exhibit a high absorption when illuminated from the other side. Moreover, when the optically transparent, weather-proofing bilayer metasurface acts as a radome, it can greatly enhance the gain and reduce RCS of the solar panel-integrated microstrip antenna without affecting the performance of optical devices (e.g., photovoltaic panels, flat panel displays, or light emitting devices). We provide the analytical formulation and design guidelines for the bilayer metasurface and the integrated cavity antenna. Our experimental results show that the realized gain of the microstrip antenna can be increased by 6.1 dBi and its RCS can be reduced by more than 20 dB around the operating frequency of 8.1 GHz. The proposed low-profile, flexible, hydrophobic, and optically transparent bilayer metasurface may be beneficial for many applications, including the next-generation radomes, self-powered 5G/6G base stations, satellite communication (CubSat), and other compact, multifunctional RF and microwave modulus integrated with optical sensors, lidar, displays, and solar panels.**

***Index Terms*— Fabry–Perrot cavity (FPC) antennas, metasurfaces, radar cross section (RCS) reduction, radomes, transparent antennas.**

I. Introduction

METASURFACES have gained significant research attention in the past few years due to their exceptional properties and remarkable abilities to control the pattern [1], polarization [2], [3], [4], focal distance [5], [6], and wavefront [7] of scattered and radiated fields, with applications spanning a broad electromagnetic spectrum. In particular, substantial efforts have been made toward achieving unidirectional or coherent perfect absorption [8], [9], [10], [11], scattering cancellation [12], [13], [14], and breaking the symmetry of absorption and reflection [15], which may open up new opportunities for the design of antennas, stealth radomes, and perfect absorbers for electromagnetic interference (EMI) and measurement applications [16], [17], [18], [19], [20], [21]. In this context, how to make high-gain antennas, while preserving low radar cross section (RCS) for suppressing multipath scattering and interferences, is a practical challenge faced by antenna engineers and has been an active area of study. To date, several methods have been studied to construct artificial surfaces that can reduce the antenna's RCS [22], [23], [24]; examples include passive frequency selective surfaces (FSSs) or metasurfaces loaded with resistive elements [25], artificial magnetic conductor (AMC) structures [26], [27], and multilayered structures that allow passive phase cancellation [28]. However, these structures may not provide gain enhancement for the antenna enclosed by them. On the other side, partially reflective surface (PRS), typically with symmetric reflectances, has been long used to enhance the gain of planar antennas (i.e., cavity antennas) [29], [30], [31], [32], [33], [34], [35], [85]. Recently, metasurfaces that simultaneously allow gain enhancement and RCS reduction of the FPC antenna have been studied [36], [37], [38], [39]. These metasurfaces are usually based on multilayer structures, of which the geometry of elementary inclusions is numerically optimized to break the symmetry of absorption, necessary for achieving the two desired functions with a low-profile structure.

In this article, we further propose an optically transparent bilayer metasurface to enhance the gain and reduce the scattering footprint of the multifunctional planar antenna integrated with optical and optoelectronic modulus (e.g., a transparent/opaque microstrip antenna placed on top of the solar panel or display), as shown in Fig. 1. Noteworthily, the appearance of such an unseeable protective radome does not affect the operating frequency and bandwidth of the covered antenna. Specifically, this work provides the analytical formulation and design guidelines for the bilayer metasurface radome made of transparent conductive films (TCFs). As illustrated in Fig. 1, the proposed transparent metasurface has high absorption and nearly zero reflection, when illuminated by microwave radiation incident from the top side. On the other hand, it has a high reflectance when illuminated by microwave incident from the bottom. As a result, the metasurface and the solar panel-integrated microstrip antenna, which

Manuscript received 24 August 2021; revised 29 August 2022; accepted 28 September 2022. Date of publication 25 October 2022; date of current version 19 January 2023. This work was supported by the NSF Electrical, Communications and Cyber Systems-Communications, Circuits, and Sensing Systems (ECCS-CCSS) under Grant 1914420. *(Corresponding author: Pai-Yen Chen.)*

Trung D. Ha, Liang Zhu, Nabeel AlSaab, and Pai-Yen Chen are with the Department of Electrical and Computer Engineering, University of Illinois at Chicago, Chicago, IL 60607 USA (e-mail: pychen@uic.edu).

Jay L. Guo is with the Department of Electrical Engineering, University of Michigan, Ann Arbor, MI 48109 USA (e-mail: guo@umich.edu).

Color versions of one or more figures in this article are available at https://doi.org/10.1109/TAP.2022.3215247.

Digital Object Identifier 10.1109/TAP.2022.3215247

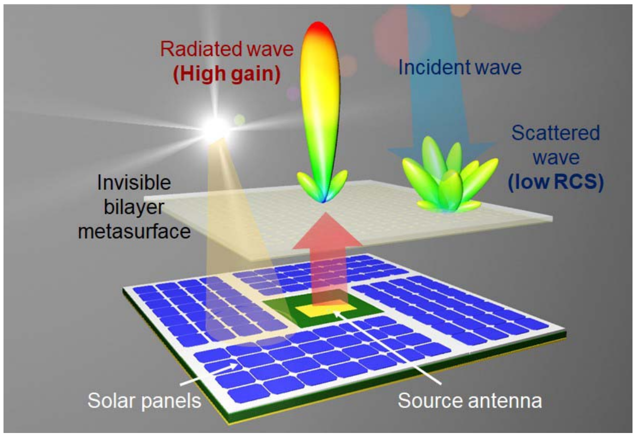

Fig. 1. Schematics of the optically transparent bilayer metasurface radome, which not only protects the source antenna (microstrip antenna here) from dust and rain but also enhances its gain and reduces the total RCS. Such a high-performance optically transparent radome may be particularly beneficial for multifunction antennas integrated with optical and optoelectronic modulus (e.g., optical sensing, lighting, displaying, communication, and energy harvesting devices).

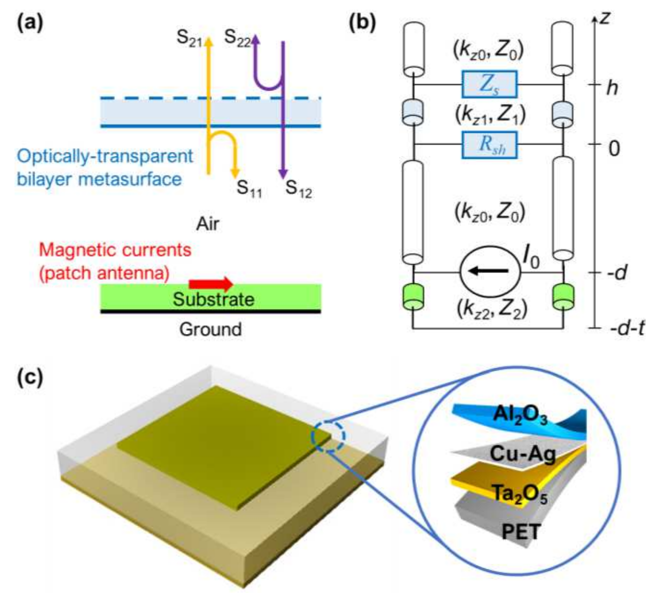

Fig. 2. (a) Side view. (b) Corresponding equivalent transmission line model of the cavity antenna formed by the transparent bilayer metasurface radome and the microstrip antenna source. (c) Unit cell of the bilayer metasurface in (a), which consists of a smooth TCF and square patch based on the same material, which are separated by a thin acrylic layer.

are separated by a suitable air gap, can effectively form a Fabry–Perot resonant structure exhibiting a highly directive broadside radiation, greatly improving the gain of the source antenna. Since the specific optically transparent TCF has antiaging and hydrophobic properties, the metasurface radome can also protect its covered antenna from rain, wind, and dust. The high-performance transparent radome may find many applications in the next-generation wireless communications systems (i.e., 5G and beyond), such as the solar-powered directive base stations [40], [41], [42], window- or mirror-embedded antennas [43], [44], CubeSat and SWaP satellite communication [45], [46], [47], [48], antenna-on-display (AoD) technologies [49], wearable electronics [50], [51], [52], and transparent antennas for vehicle communications and the Internet of Things (IoTs) [53], [54], [55].

This article is organized as follows. Section II presents the analytical formulation and systematic design approach for the transparent bilayer metasurface and high-gain, low-RCS FPC antennas formed by it. Section III reports numerical and experimental results validating the theory developed in Section II. Section III also shows the optical and hydrophobic properties of the proposed transparent bilayer metasurface for illuminating the potential of the proposed transparent bilayer metasurface in modern radome applications. Finally, a conclusion is drawn in Section IV.

II. Theoretical Design of Fabry–Perot Antenna

A. Radiation Pattern of an FPC Antenna

The concept of PRS-based FPC antenna was first introduced in [29] and analyzed using the ray-tracing method, commonly used to analyze a resonant optical cavity formed by Fabry–Perot interferometer [56], [57], [58]. In the RF and microwave regime, a highly reflective surface (e.g., metasurface) and a ground plane resemble the reflection surfaces, as shown in Fig. 1. The FPC antenna is generally excited by a source antenna (e.g., microstrip patch or wire antenna) placed within the cavity, such that waves radiated by the source bounce back and forth between the ground plane and the PRS, resulting in the resonant transmission. In this case, a phase shift is introduced by the path length, the phase of the reflection coefficient of the PRS ϕ_1, and that of the grounded dielectric slab ϕ_2. The sum of the partially transmitted rays yields a directive radiation pattern, and for a given angle θ, the transmitted power can be explicitly expressed as follows:

$$\begin{aligned} P(\theta) &= \left|\frac{S_{21}(\theta)}{1-S_{11}(\theta)\times\exp(j\phi_2(\theta)-jk_0d\cos\theta)}\right|^2\times F^2(\theta) \\ &= \left[\frac{1-|S_{11}(\theta)|^2-A_B}{1+|S_{11}(\theta)|^2-2|S_{11}(\theta)|\cos\Phi}\right]\times F^2(\theta) \end{aligned} \quad (1)$$

where S_{11}, S_{21}, and A_B are the complex-valued reflection coefficient, transmission coefficient, and absorptivity of bilayer metasurface for bottom side incidence, as given in Fig. 2(a), k_0 is the free-space wavenumber, d is the distance between the bilayer metasurface and the grounded dielectric slab, $\Phi = \phi_1(\theta)+\phi_2(\theta)-2k_0d\cos\theta$, $\phi_1(\phi_2)$ is the phase of reflection coefficient of the PRS (grounded dielectric slab), and $F(\theta)$ is the radiation pattern of the source antenna. The first term in (1) can be regarded as a gain enhancement factor, namely, the total gain relative to the gain of the source antenna. For a given angle θ, the maximum radiated power is achieved when the following condition is satisfied [59]:

$$\phi_1(\theta)+\phi_2(\theta)-\frac{4\pi}{\lambda_0}d\cos\theta = 2N\pi,\ \text{where}N = 0, 1, 2, 3, \ldots \quad (2)$$

where λ_0 is the free-space wavelength and the phase of reflection coefficient of the grounded dielectric slab is given as

$$\phi_2(\theta) = \angle \frac{-Z_0 + jZ_2 \tan(k_{Z_2} t)}{Z_0 + jZ_2 \tan(k_{Z_2} t)} \quad (3)$$

where Z_0 and Z_2 are the characteristic impedance of air and that of the dielectric substrate with relative permittivity ε_2 and thickness t, and $k_{Z_2} = k_0(\varepsilon_2 - \sin^2\theta)^{1/2}$ is the longitudinal wavenumber of plane waves inside the dielectric slab, as shown in Fig. 2(b). For TE^Z and TM^Z polarizations, the characteristic impedances of the dielectric substrate are given by: $Z_0^{\mathrm{TE}} = \eta_0 \sec\theta$, $Z_0^{\mathrm{TM}} = \eta_0 \cos\theta$, $Z_2^{\mathrm{TE}} = \eta_0/(\varepsilon_2 - \sin^2\theta)^{1/2}$, and $Z_2^{\mathrm{TM}} = \eta_0(\varepsilon_2 - \sin^2\theta)^{1/2}/\varepsilon_2$, and η_0 is the impedance of free space. If the inherent material losses of the bilayer metasurface are moderately low, the broadside gain relative to that of the source antenna can be approximately written as

$$G(0) = \frac{P(0)}{F(0)} = \frac{1 + |S_{11}(0)|}{1 - |S_{11}(0)|}. \quad (4)$$

We know from (4) that the antenna gain would increase with the increase of the reflection magnitude of the bilayer metasurface.

B. Bilayer Metasurface With Asymmetric Absorption

The characteristics of the metasurface formed by the transparent conductive patch array and the bottom TCF [see Fig. 2(c)] can be described by a homogeneous and isotropic surface impedance $Z_S = R_S + jX_S$ and a uniform sheet resistance R_{sh} (here, $R_{sh} = 11\ \Omega$/sq), respectively, as shown in Fig. 2. The shunt impedances, Z_s and R_{sh}, are separated by a short segment of transmission line, with an electrical distance $x = k_0 h(\varepsilon_1 - \sin^2\theta)^{1/2}$, where ε_1 and h are the relative permittivity and thickness of the dielectric spacer (acrylic) supporting the transparent metasurface and the TCF (here, $\varepsilon_1 = 2.6$ with a loss tangent $\tan\delta = 0.025$ and $h = 1.5$ mm). By using the transfer matrix method [60], the reflection coefficients of the bilayer metasurface can be written as

$$S_{11} = \frac{\begin{array}{c}-\left[Z_0^2 Z_S R_{sh} + Z_1^2(Z_0 + Z_S)(Z_0 - R_{sh})\right]\sin(x) + \\ +jZ_1 Z_0^2(Z_S + R_{sh})\cos(x)\end{array}}{\begin{array}{c}\left[Z_0^2 Z_S R_{sh} + Z_1^2(Z_0 + Z_S)(Z_0 + R_{sh})\right]\sin(x) - \\ -jZ_1^2 Z_0[2Z_S R_{sh} + Z_0(Z_S + R_{sh})]\cos(x)\end{array}} \quad (5a)$$

and

$$S_{22} = \frac{\begin{array}{c}-\left[Z_0^2 Z_S R_{sh} + Z_1^2(Z_0 - Z_S)(Z_0 + R_{sh})\right]\sin(x) + \\ +jZ_1 Z_0^2(Z_S + R_{sh})\cos(x)\end{array}}{\begin{array}{c}\left[Z_0^2 Z_S R_{sh} + Z_1^2(Z_0 + Z_S)(Z_0 + R_{sh})\right]\sin(x) - \\ -jZ_1^2 Z_0[2Z_S R_{sh} + Z_0(Z_S + R_{sh})]\cos(x)\end{array}}. \quad (5b)$$

Since the system is reciprocal, the scattering matrix $S = S^T$ and transmission are symmetric, yielding

$$S_{21} = S_{12} = \frac{-2jZ_1 Z_0 Z_S R_{sh}}{\begin{array}{c}\left[Z_0^2 Z_S R_{sh} + Z_1^2(Z_0 + Z_S)(Z_0 + R_{sh})\right]\sin(x) - \\ -jZ_1^2 Z_0[2Z_S R_{sh} + Z_0(Z_S + R_{sh})]\cos(x)\end{array}} \quad (6)$$

where the characteristic impedances of the dielectric spacer are $Z_1^{\mathrm{TE}} = \eta_0/(\varepsilon_1 - \sin^2\theta)^{1/2}$ and $Z_1^{\mathrm{TM}} = \eta_0(\varepsilon_1 - \sin^2\theta)^{1/2}/\varepsilon_1$. In order to suppress RCS to make a stealth antenna, while at the same time enhancing the maximum gain of the source antenna at broadside, a bilayer metasurface must be properly designed to achieve asymmetric reflection and absorption, with $S_{11}(0) \approx e^{j\pi}$, $S_{22}(0) \approx 0$, $S_{21}(0) \approx 0$, and $S_{12}(0) \approx 0$, which lead to absorptivities given by $A_T(0) = 1 - |S_{22}(0)|^2 - |S_{12}(0)|^2 \approx 0$ and $A_B(0) = 1 - |S_{11}(0)|^2 - |S_{21}(0)|^2 \approx 1$. Given the sheet resistance of TCF R_{sh}, the ideal surface impedance set of the bilayer metasurface that makes $S_{11}(0) = -1$ and $S_{22}(0) = S_{21}(0) = S_{12}(0) = 0$ at normal incidence can be derived. In this case, the surface resistance and surface reactance of the top layer consisting of the TCF patch array are given by

$$R_S = \frac{(1+\gamma)\left[1 + \gamma(1-\varepsilon_1)\right]\tan^2(x) - \varepsilon_1\gamma}{\varepsilon_1 + \left[1 + \gamma(1-\varepsilon_1)\right]^2\tan^2(x)} Z_0 \quad (7a)$$

$$X_S = -j\frac{1 + 2\gamma + \gamma^2(1-\varepsilon_1)}{\sqrt{\varepsilon_1}\cot(x) + (1 + \gamma - \varepsilon_1\gamma)^2\tan(x)/\sqrt{\varepsilon_1}} Z_0 \quad (7b)$$

where $\gamma = R_{sh}/Z_0$. If the TFC is lossless [i.e., $S_{11}(0) \approx e^{j\pi}$] and the electrical distance between the TCF and the TCF patch array is $x = \pi/2$ (i.e., $h = \lambda_0/4(\varepsilon_1)^{1/2}$), the optimum surface impedance is given by $Z_s = Z_0$, as if the structure acts as a Salisbury screen that absorbs uniform plane wave normally incident upon the top surface. For the illustration purpose, we assume a TCF with very low sheet resistance (i.e., $\gamma \ll 1$) and a thin dielectric spacer with subwavelength thickness (i.e., $k_0 h \ll 1$, such that $\tan x \simeq x$). In this quasi-static approximation, the optimum surface impedance of the metasurface can be expressed as

$$Z_S = \left[\frac{1}{1 + (k_0 h)^{-2}} - j\frac{k_0 h}{1 + (k_0 h)^2}\right] Z_0 \approx \left[(k_0 h)^2 - jk_0 h\right] Z_0. \quad (8)$$

From (8), we know that a lossy, capacitive metasurface should be utilized to compensate the inductive nature of the input impedance looking into the metasurface $Z_{in} = j(Z_0/(\varepsilon)^{1/2})\tan((\varepsilon)^{1/2}k_0 h) \approx jk_0 h Z_0$. In general, for a TCF with moderately low conduction loss, a capacitive top metasurface is required to reduce the antenna's RCS at the frequency of interest.

For the 2-D conductive patch array in Fig. 2(c), the equivalent surface impedance can be explicitly written as [61], [62], [63]

$$Z_S = \frac{1}{1-\xi} R_{sh} - j\frac{Z_0}{\varepsilon_{eff}\,\psi\,\ln[\csc(\pi\xi/2)]}\varphi(\theta) \quad (9)$$

where $\psi = 4p/\lambda_0$, $\xi = g/p$, p is the unit cell period, g is the gap size, $\varepsilon_{\mathrm{eff}} = (\varepsilon_1 + 1)/2$ is the averaged relative permittivity of the upper and lower media, ε_1 is the relative permittivity of the host substrate, and $\varphi_{TM}(\theta) = 1$ and $\varphi_{TE}(\theta) = 1 - \sin^2\theta/(2\varepsilon_{\mathrm{eff}})$ are the angular correlation functions for the TM- and TE-polarized incident waves, respectively. Equation (9) is valid for wavelength and incident angles that satisfy the condition $\psi(1 + \sin\theta)/4 < 1$. At the normal incidence, the surface impedance of $Z_S = R_S + jX_S$

described in (7) can be obtained by choosing the geometric parameters, g and p, to be

$$g = \left(1 - \frac{R_{sh}}{R_S}\right) p \tag{10a}$$

$$p = -j \frac{Z_0/X_S}{(\varepsilon_1 + 1)\ln[\csc[\pi(1 - R_{sh}/R_S)/2]]} \frac{\lambda}{2}. \tag{10b}$$

If the slab thickness h is less than $0.3p$, the evanescent mode coupling between the metasurface and TCF should be taken into consideration, and (9) should be modified as [64], [65]

$$Z_S = \frac{1}{1-\xi} R_{sh} - j \frac{Z_0}{\varepsilon_{eff}\,\psi(\ln[\csc(\pi\xi/2)] - \ln(1 - e^{-4\pi h/p}))} \varphi(\theta). \tag{11}$$

Given the material properties of the TCF, $R_{sh} = 11$ Ω/sq and $\varepsilon_1 = 2.6$, the geometric parameter of the top grid array of the bilayer metasurface can be obtained from (7) and (10) as $p = 11.9$ mm and $g = 9.5$ mm, which results in a surface impedance of $Z_S = 43.54 + j\,97.0978$ Ω at 8.1 GHz. Moreover, considering a metal-backed Roger RO4350B substrate with dielectric constant $\varepsilon_2 = 3.66$ and thickness $t = 1.5$ mm, the reflection phase $\angle\phi_2(0)$ given by (3) is 147.2°. The reflection phase of the transparent patch array is $\phi_1(0) = 2\pi$ at 8.1 GHz [see (5)]. Therefore, the air-gap size enabling the resonance at 8.1 GHz can be obtained from (1) as $h = 18$ mm. At 8.1 GHz, the magnitude of reflection coefficient of the grounded substrate and the bilayer metasurface are calculated to be 1 and 0.91836, which lead to a maximum relative gain of 12.78 dBi at broadside. Therefore, when the source microstrip antenna with the realized gain of 6.8 dBi is covered with the above unseeable bilayer metasurface radome of infinite size, its realized gain can be increased to 19.6 dBi.

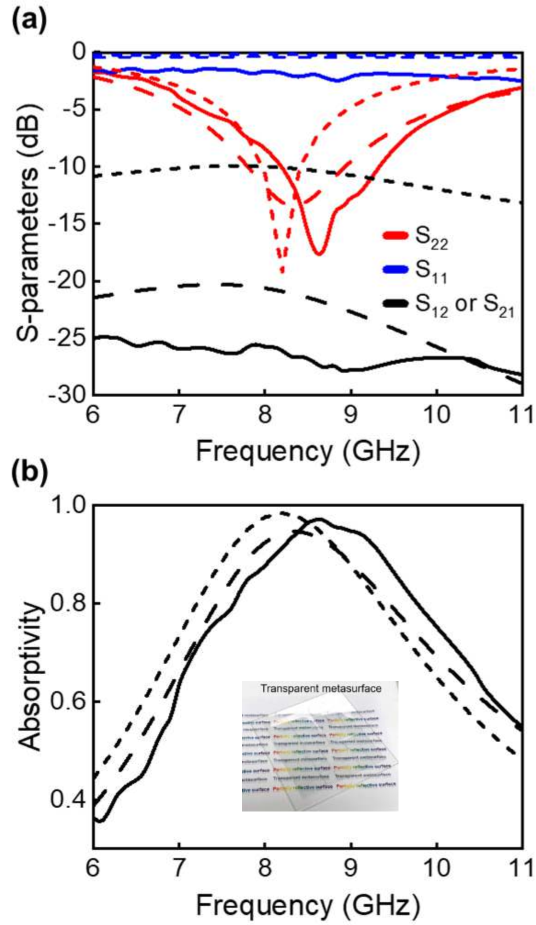

Fig. 3. Analytical (dotted line), numerical (dashed line), and experimental (solid line) results of (a) scattering parameters of the optically transparent radome in Fig. 2. (b) Absorptivity under normal incidence from the bottom side; the inset in (b) shows the fabricated transparent bilayer metasurface.

III. Results and Analysis

We have conducted the full-wave simulation based on the frequency-domain finite-element method considering all Floquet modes [66] to validate the analytical analysis presented in Section II. Due to the rapid advance of nanofiltration and nanomaterials, so far, several TCFs have been synthesized, including transparent conductive oxides (i.e., indium tin oxide (ITO) [67], [68], [69]), nanocarbon [70], and conductive polymer [71]. Furthermore, we also have fabricated the prototype of optically transparent bilayer metasurface radome based on our recently developed doped nanometal film [72], [73], [74], [75]; here, the top TCF was patterned into the square-patch array using the CO_2 laser engraving cutter, which together with the ground transparent conductive sheets, were attached to a 10 cm × 10 cm × 1.5 mm acrylic substrate. On the top side of the fabricated bilayer metasurface, there are 8 × 8 square patches. Fig. 3(a) reports the S-parameters of the transparent bilayer metasurface [see Fig. 2(a)]. We find that there is a good agreement between analytical, numerical, and measurement results. The low transmission (S_{12}) and reflection (S_{22}) around the operating frequency (8.1 GHz) are obtained when illuminated by normally incident plane wave from the top half-space, which implies a high absorption and thus low RCS. On the other hand, low transmission and high reflection (S_{11}) are obtained in the same frequency range under normal illumination from the bottom half-space; such a property can be exploited to build a high-gain cavity antenna with a directive broadside radiation pattern. From the measured S-parameter, we can compute the absorption of bilayer metasurface, given by [59], [60]

$$A_T = 1 - |S_{22}|^2 - |S_{12}|^2 \tag{11a}$$

$$A_B = 1 - |S_{11}|^2 - |S_{21}|^2 \tag{11b}$$

where A_T and A_B are the absorptivity for normal illumination form the top and bottom half-spaces.

Fig. 3(b) presents the asymmetric absorption of the bilayer metasurface radome, showing a good agreement between the theoretical and measurement results. We note that there is ∼2 dB discrepancy due primarily to the finite size of the fabricated structure. From the measurement results, we find that a high reflection of 91.57% reflection and a high absorption of 97.21% at 8.1 GHz are obtained from normal incidence from the bottom and top sides. Such highly asymmetric

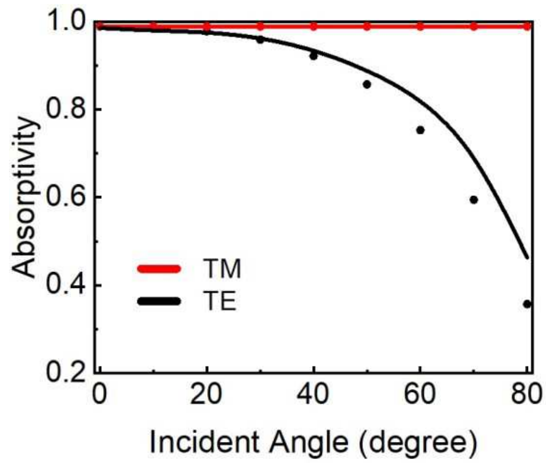

Fig. 4. Analytical (solid lines) and numerical (dots) results for the dependence of absorptivity on the incident angle of TE (black) and TM (red) polarized waves.

reflective/absorptive properties play a key role in making low-RCS and high-gain radome-covered multifunctional antenna.

Here, we note that since the bilayer metasurface is ultrathin and the input impedance looking into the top surface is rather insensitive to the angle of incidence (particularly for the TM-polarized incident wave [see (11)]), the RCS reduction effect could be independent of the angle of incidence. Fig. 4 reports the analytical and simulated absorptivity versus the incident angle at 8.1 GHz for TE- and TM-polarized waves incident upon the top surface. It can be clearly seen that the analytical results are in good agreement with simulated ones, and both results indicate that the wide-angle absorption can be achieved for both TE and TM polarizations. This implies that the RCS reduction can be effective over a wide range of incident angles and be polarization independent. For large incident angles, there is a certain difference between the analytical results and the numerical results, as shown in Fig. 4. The accuracy of analytical analysis for obliquely incident plane waves can be improved by considering higher order Floquet modes (spatial harmonics), i.e., the surface impedance may comprise the Floquet expansion terms that are usually ignorable under normal incidence [76], [77]. The results presented in Fig. 4 are consistent with (11), which predicts an incident angle-independent Z_s for the TM polarization, whereas Z_s shows an angular dependency in $\varphi(\theta)$ for the TE polarization.

Fig. 5 shows the photograph of the fabricated multifunctional cavity antenna comprising the microstrip antenna, solar panels, and the unseeable radome in Fig. 3. The microstrip patch antenna used to excite the cavity structure is based on the RO4350B substrate and is fed by the 50 Ω co-axial cable. The commercial solar panels manufactured by Power Film Solar Inc., [78] comprise a thin layer of amorphous silicon p-n junction and transparent electrodes (only a few micrometers in the total thickness) grounded by a metallic contact (which is equivalent to a perfect electrical conductor or PEC boundary condition in the microwave regions). The introduction of solar panels does not affect the radiation characteristics of both

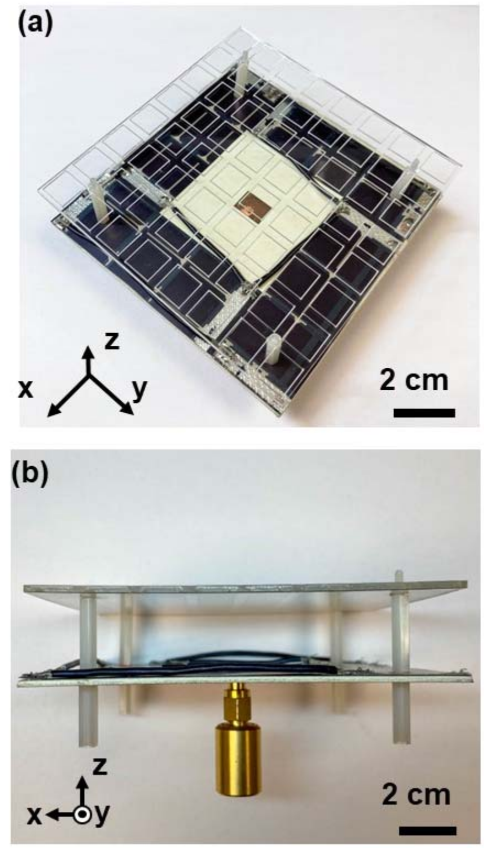

Fig. 5. (a) Perspective view. (b) Side view of the fabricated cavity antenna covered by the invisible radome in Fig. 3. The bulges are wires connecting (in parallel) electrodes of four solar panels, which have negligible effect on the performance of the antenna and solar panels.

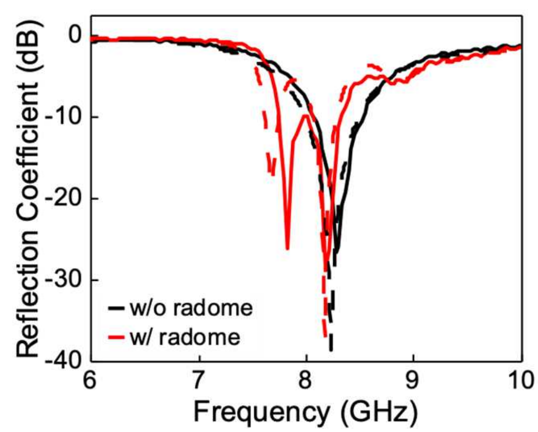

Fig. 6. Simulated and measured reflection coefficient S_{11} of patch antenna with (red) and without (black) the invisible radome; here, solid and dashed lines represent the measurement and numerical results, respectively.

source antenna and cavity. The optimum cavity height is calculated to be $h = 17.8$ mm.

Fig. 6 presents the simulated and measured reflection coefficients of the solar panel-integrated microstrip patch antenna with and without the optically transparent metasurface radome in Fig. 5. It can be seen clearly that the patch antenna (feeding source) has a resonant frequency at 8.1 GHz with a bandwidth

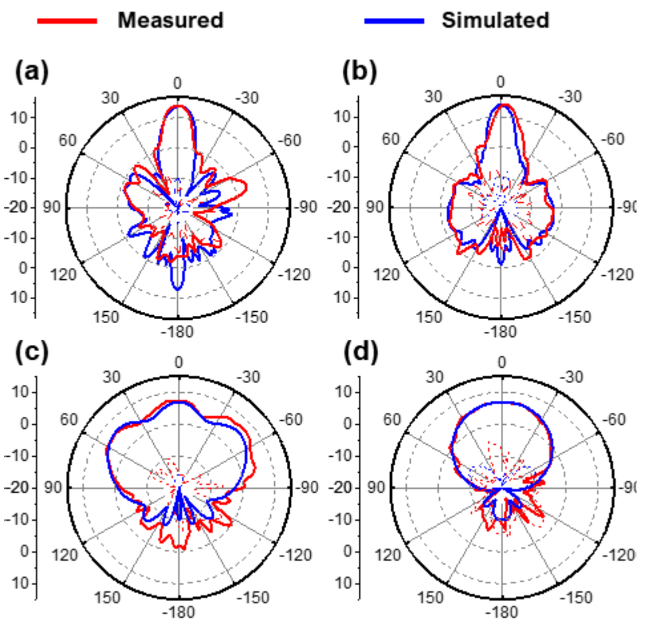

Fig. 7. Measured and simulated radiation patterns at 8.1 GHz on (a) E (x–z) plane and (b) H (y–z) plane for the solar panel-integrated microstrip antenna with the metasurface radome. (c) and (d) are similar to (a) and (b), but for the same microstrip antenna without the radome; here, the solid and dashed lines represent the co-polarization and cross-polarization patterns, respectively.

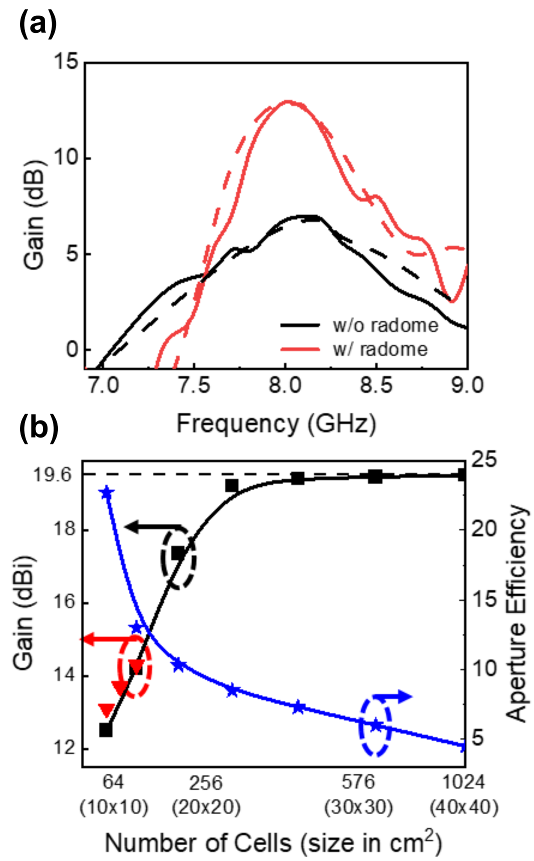

Fig. 8. (a) Simulated and measured broadside gain of the solar panel-integrated microstrip antenna with and without the metasurface radome; here, the solid and dashed lines represent the measurement and simulation results, respectively. (b) Simulated and measured broadside gain versus the number of unit cells on the top layer of the bilayer metasurface; here, the red and black symbols represent the measurement and simulation results, the solid lines are the curve-fitting results, and the dashed line is the theoretical maximum broadside gain given by (4). The simulated aperture efficiency and its fitting result are shown as blue stars and lines.

of 516 MHz, while the solar integrated antenna can resonate at similar 8.1 GHz with the bandwidth of 230 MHz. The full-wave simulation and experimental results are in a good agreement, with a slight difference due to the fabrication and measurement errors. The results in Fig. 6 show that the appearance of the radome does not influence the impedance matching property and the fundamental resonance frequency of the antenna. Fig. 7(a)–(d) presents the co-polarization and cross-polarization radiation patterns of the microstrip antenna with and without the radome at 8.1 GHz, showing that the maximum realized gain is 13.2 dBi with the radome, while it drops to 7.1 dBi without the radome. Again, the simulation and measurement results are in an excellent agreement. It can be clearly seen from Fig. 7 that the directivity and maximum (broadside) gain of the microstrip antenna can be enhanced by exploitation of the radome. At broadside, the maximum realized gain can be increased by 6.1 dBi. In addition, the undesired cross polarization levels are minimized for both cases, with a cross polarization less than -15 dB (-16 dB) on the E-plane (H-plane). Fig. 8(a) compares the maximum gain at broadside versus frequency for the microstrip antenna with and without the radome, showing that the transparent radome can effectively improve the antenna's gain in its operating frequency band centered at 8.1 GHz. It can be seen from Fig. 6(b) that there is an additional resonance due to the appearance of radome. Such an effect is also observed in opaque FPC antennas [30], [56], [79] and could be explained by Fano resonance due to interactions between two coupled resonators, resulting in bright-mode and dark-mode dips in the reflection spectrum [80], [81]. As shown in Fig. 8(a), the additional peak would disappear in the gain spectrum and, thus, can be considered as the nonradiative dark mode. We note that the measured gain is lower than the theoretical prediction for an infinitely large cavity antenna, which exhibits a broadside gain of 19.6 dBi. To answer this question, Fig. 8(b) presents the simulated broadsight gain versus frequency for the resonant cavity antenna with different dimensions, including 10×10 cm^2[see Fig. 7(a)], 15×15 cm^2, 20×20 cm^2, 25×25 cm^2, and 30×30 cm^2, which correspond to 64, 144, 256, 400, and 576 unit cells on the top side of the bilayer metasurface. The simulation results validate the analytical model, showing that the maximum gain value may approach 19.6 dBi when a large radome (i.e., a 30×30 cm^2) is used. The curve-fitting result in Fig. 8(b) shows that the broadside gain experiences saturation when the number of unit cells is greater than 400. We have also fabricated and characterized the broadside gain of the cavity antenna with different radome areas (64, 100, and 144 unit cells), and the results are reported in Fig. 8(b). It can be seen that the measurement results conform to the trend and locus predicted by the simulation results. Moreover, the analytical model can predict the upper bound well. We note that the opaque microstrip antenna as

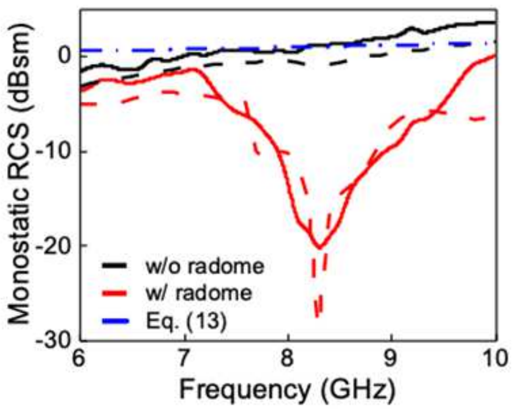

Fig. 9. Monostatic RCS of the microstrip antenna with and without the radome; here, the solid and dashed lines represent the measured and simulated results, respectively, and the dashed-dotted is the maximum RCS for a metallic plate, which is given by (13).

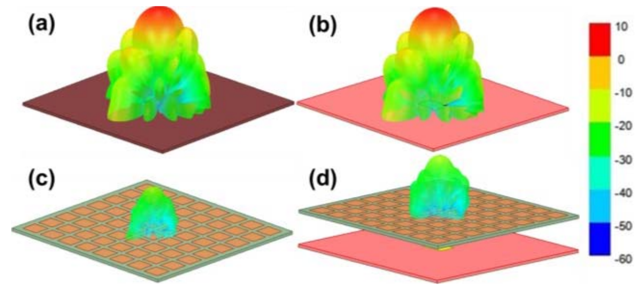

Fig. 10. Simulated 3-D monostatic RCS pattern at 8.1 GHz for (a) metallic plate reference, (b) patch antenna, (c) bilayer metasurface, and (d) low-RCS, high-gain cavity antenna comprising the patch antenna in (b) and the bilayer metasurface in (c); units: dBsm.

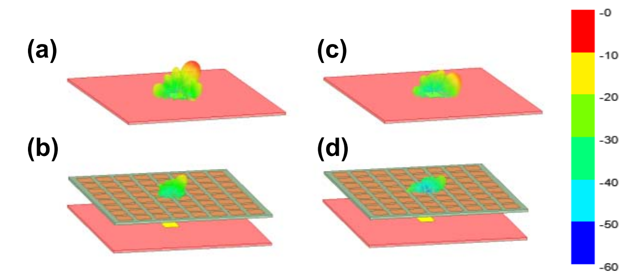

Fig. 11. Simulated 3-D RCS pattern for the TM-polarized plane wave obliquely incident at 30° and 60° on (a) and (c) patch antenna and (b) and (d) metasurface radome-covered patch antenna; units: dBsm.

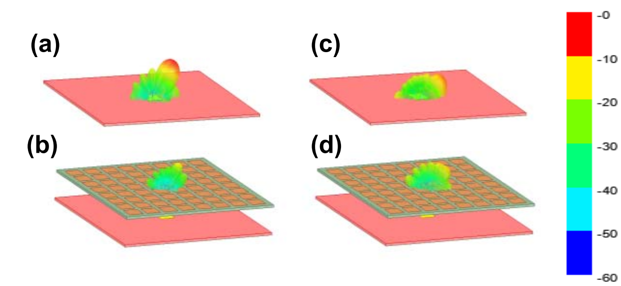

Fig. 12. Simulated 3-D RCS pattern of the patch antenna (a) without and (b) with the metasurface radome when illuminated by the obliquely incident TE-polarized plane wave illumination at 30°. (c) and (d) Similar to (a) and (b), but with an incident angle of 60°; units: dBsm.

a feeding source can be replaced with a transparent planar antenna to construct a fully transparent and flexible FPC antenna, where the gain-enhancing metasurface radome can compensate the low radiation efficiency of the transparent source antenna. Fig. 8(b) also presents the aperture efficiency of the antenna, defined as [82]

$$\varepsilon_A = \frac{A_{eff}}{A_p} = \frac{\lambda^2 G}{4\pi A_p} \tag{12}$$

where A_{eff} is the effective area, A_p is the physical area, and G is the maximum realized gain. It can be observed from Fig. 8(b) that the aperture efficiency decreases with increasing the number of unit cells and starts to saturate when more than 400 unit cells are used. The trend of aperture efficiency obtained from simulations is consistent with that of the measured maximum broadside gain plotted in the same figure; namely, the maximum gain is locked to the physical limit when a large number of elements are used. In addition, at 8.1 GHz, the simulated radiation efficiencies of the Fabry–Perot antennas are 80.73%, 73.53%, and 69.9% for the metasurfaces with dimensions of 10 × 10, 20 × 20, and 30 × 30 cm^2, respectively.

In this work, we also conducted monostatic RCS measurements for the microstrip antenna and the cavity antenna in the anechoic chamber. In the RCS characterization, the antennas were connected to a 50 Ω match load, and a square metallic plate of the same size was used as a reference whose RCS value is given by [60]

$$\sigma = \frac{4\pi a^4}{\lambda_0^2} \tag{13}$$

where a is the width of the square metallic plate. Fig. 9 presents the broadside RCS for the microstrip antenna with and without the anti-RCS radome in Fig. 5. It is evident that the radome can effectively reduce the RCS of microstrip antenna by more than 10 dB in the frequency range of interest (7.5–9 GHz). An uncovered microstrip antenna displays a relatively large RCS comparable to that of the metallic plate of the same size. The simulation results also agree well with the measurement results, as can be seen in Fig. 9. Fig. 10 compares the simulated 3-D monostatic RCS patterns for the metallic reference plane, the bilayer metasurface, the patch antenna, and the low-RCS, high-gain cavity antenna comprising the bilayer metasurface and the patch antenna. It can be seen that the RCS values of the patch antenna [see Fig. 10(b)] are comparable to those of the metallic reference plane [see Fig. 10(a)] and can be significantly reduced by adding the bilayer metasurface [see Fig. 10(d)]. Table I presents a detailed comparison between the proposed transparent metasurface radome and the previously reported (opaque) metasurface radomes for high-gain and low-RCS antenna applications. We find that the proposed antenna, although being optically transparent, can have a gain that is close to the opaque ones with similar dimensions and operating frequencies.

Fig. 11 reports the variations of the simulated RCS with the angle of incidence (bistatic measurement) under the TM-polarized illumination at 8.1 GHz. It is evident that the RCS is low over a wide angular range. Similar scattering

TABLE I
SUMMARY OF METASURFACE RADOMES FOR LOW RCS AND HIGH-GAIN ANTENNA APPLICATIONS

Reference	Antenna source	Resonant Freq.	Superstrate transparency	Size (cm^2)	Peak Gain (dBi)	RCS reduction	Photovoltaic
[23]	Slot	5.62 GHz	Opaque	12x12	9.5	15 dB	N/A
[24]	Array	10 GHz	Opaque	11x11	17.9	10 dB	N/A
[37]	Patch	10 GHz	Opaque	11x11	18.4	13 dB	N/A
[38]	Patch	10 GHz	Opaque	11x11	19.8	20 dB	N/A
[39]	Patch	10.7 GHz	Opaque	7.5x7.5	10.2	27.9 dB	N/A
Proposed	Patch	8.1 GHz	88.1 %	10x10 (25x25)	13.1 (19.4)	20 dB	Yes

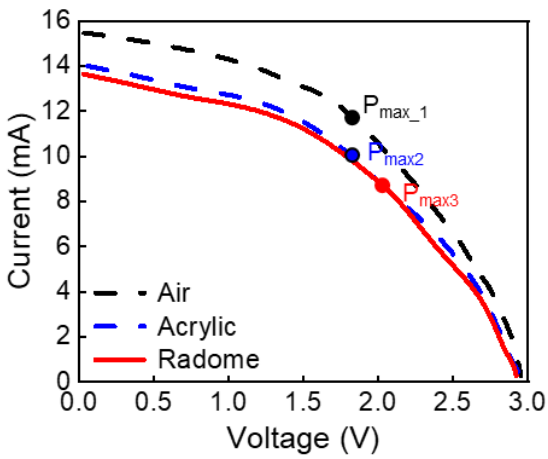

Fig. 13. Photovolatic performance of the solar panel suspended in air (black line) and covered by the optically transparent metasurface radome (red line) and the acrylic substrate (blue line); here, P_{max_1}, P_{max_2}, and P_{max_3} are the peak performance of solar panel illuminated from light source through air, acrylic, and radome, respectively.

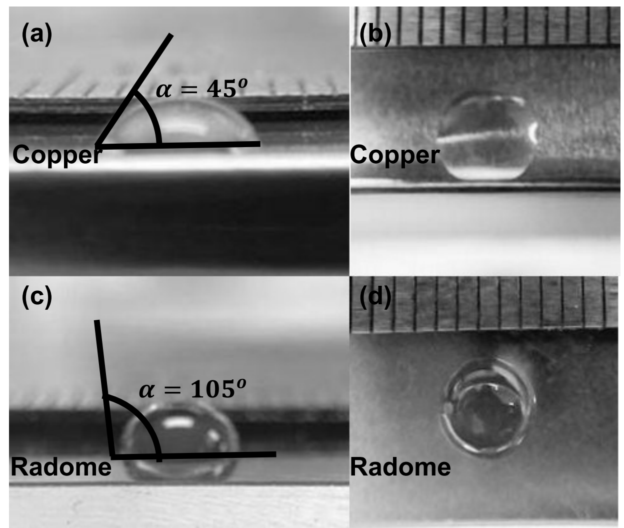

Fig. 14. (a) Side view and (b) top view of a water drop on the copper patch surface. (c) and (d) are similar to (a) and (b), but for the hydrophobic metasurface radome.

reduction effect is also obtained for the TE polarization, as can be seen in Fig. 12. The simulation results basically agree with the analytical absorptivity plotted in Fig. 4. For TM polarization, the effect of RCS reduction is moderately wideband and robust against changes in the incident angle, as a high absorptivity can be obtained over a wide angular range up to endfire [see Fig. 4]. The RCS reduction is also effective for TE polarization, but with degraded (yet satisfactory) performance at endfire, consistent with the analytical results in Fig. 4.

Finally, we also studied the optical and hydrophobic properties of the fabricated bilayer metasurface radome made of our recently proposed doped nanometal film [72], [73], [74], [75]. Fig. 13 reports the measured current–voltage characteristics of the solar panel placed in air and underneath the 1.5 mm thick acrylic substrate and the optically transparent metasurface radome of the same thickness. These solar panels were connected in parallel by jumper wires to cover the proximity of the microstrip antenna. It is seen from Fig. 13 that all three cases display similar maximum conversion efficiency, short-circuit current, and open-circuit voltage. Under the standard illumination at 6 mW/cm^2, the maximum generated electric power is ~21.42, 19.45, and 18.90 mW for the air-, acrylic-, and radome-covered solar panel. We note that the small difference in the photovoltaic efficiency between air and the acrylic substrate is attributed to the slight refractive index mismatch between these two media. Comparing the photovoltaic performance between the acrylic substrate and the radome, it is clearly evidence that the appearance of the top and bottom conductive layers with an averaged optical transparency of 88.1% in the visible range may have a little and almost ignorable effect on the optical transmittance. In other words, the transparent protective radome does not affect the performance of optical and optoelectronic properties underneath it. It is worth noting that at X-band, Xi et al. [83] and Zarbakhsh et al. [84] had also implemented the integrated photovoltaic antennas, which can have high gain and provide the photovoltaic energy harvesting. However, these antennas have larger dimensions and RCS values than those reported in this work.

To understand the hydrophobic properties (i.e., water vulnerability) of the protective radome, we have conducted a simple hydrophobic angle test. In this experiment, water droplet was injected from a syringe into the surface of copper microstrip patch [see Fig. 14(a) and (b)] and the top surface of the radome [see Fig. 14(c) and (d)]. When a water droplet is attached to the copper surface, it quickly flattens due to the surface tension with a contact angle of 45°, as can be seen in Fig. 14(a) and (b). On the other hand, the water droplet, when attached on the TCF coated with hydrophobic antireflection layer, the droplet remains in a stable, hydrophobic shape with a contact angle of 105°, as can be seen in Fig. 14(c) and (d). The test validates that the proposed radome can be weather-proof and sufficiently transparent, such that the covered antenna and optical device can be protected without sacrificing their performance in the optical domain.

IV. Conclusion

In summary, we have proposed design and analytical formulation for a compact, lightweight, and optically transparent bilayer metasurface exhibiting extreme asymmetry in microwave reflection and absorption. Such an invisible bilayer metasurface with exotic electromagnetic properties, when used as a radome, may effectively increase the gain and reduce the RCS of the covered multifunctional antenna modulus without affecting its optical or optoelectronic performance. As a representative example, we have theoretically and experimentally studied an FPC antenna consisting of a microstrip antenna (radiation source) and the proposed transparent radome based on our recently manufactured transparent and conductive nanometal composite. Our results have demonstrated that the finite-size transparent radome (10×10 cm^2) can effectively increase the broadside gain of the microstrip patch antenna by 6.1 dBi at 8.1 GHz, while reducing its RCS by more than 10 dB in the frequency range between 7.5 and 9 GHz. The gain enhancement may be further improved by increasing the area of radome. Moreover, this hydrophobic weatherproof radome has nearly ignorable effect on the photovoltaic performance of the solar panel surrounding the radiative microstrip. Finally, we note that this optically transparent gain-enhanced radome can be exploited to compensate the relatively low radiation efficiency of the existing transparent antennas, thus facilitating the practice of transparent wireless electronics with multifunction integration with optoelectronic devices, displays, or solar panels. We envision that the proposed optically transparent bilayer metasurface may be of great interest for the next-generation wireless communication in emerging applications, such as the self-powered 5G/6G wireless network, CubeSats, AoD technology, smart glasses, and smart cities.

References

[1] P.-S. Kildal, "Artificially soft and hard surfaces in electromagnetics," *IEEE Trans. Antennas Propag.*, vol. 38, no. 10, pp. 1537–1544, Oct. 1990.

[2] G. Minatti, F. Caminita, E. Martini, M. Sabbadini, and S. Maci, "Synthesis of modulated-metasurface antennas with amplitude, phase, and polarization control," *IEEE Trans. Antennas Propag.*, vol. 64, no. 9, pp. 3907–3919, Sep. 2016.

[3] X. F. Zang et al., "Polarization encoded color image embedded in a dielectric metasurface," *Adv. Mater.*, vol. 30, no. 21, May 2018, Art. no. 1707499.

[4] C. Pfeiffer and A. Grbic, "Millimeter-wave transmitarrays for wavefront and polarization control," *IEEE Trans. Microw. Theory Techn.*, vol. 61, no. 12, pp. 4407–4417, Dec. 2013.

[5] M. F. Imani, T. Sleasman, and D. R. Smith, "Two-dimensional dynamic metasurface apertures for computational microwave imaging," *IEEE Antennas Wireless Propag. Lett.*, vol. 17, no. 12, pp. 2299–2303, Dec. 2018.

[6] M. F. Imani et al., "Review of metasurface antennas for computational microwave imaging," *IEEE Trans. Antennas Propag.*, vol. 68, no. 3, pp. 1860–1875, Mar. 2020.

[7] Y. Ra'di, D. L. Sounas, and A. Alù, "Metagratings: Beyond the limits of graded metasurfaces for wave front control," *Phys. Rev. Lett.*, vol. 119, no. 6, Aug. 2017, Art. no. 067404.

[8] P.-Y. Chen, M. Farhat, and H. Bağci, "Graphene metascreen for designing compact infrared absorbers with enhanced bandwidth," *Nanotechnology*, vol. 26, no. 16, Apr. 2015, Art. no. 164002.

[9] P. Chen and A. Alù, "Terahertz metamaterial devices based on graphene nanostructures," *IEEE Trans. THz Sci. Technol.*, vol. 3, no. 6, pp. 748–756, Nov. 2013.

[10] M. Farhat, M. Yang, Z. Ye, and P.-Y. Chen, "PT-symmetric absorber-laser enables electromagnetic sensors with unprecedented sensitivity," *ACS Photon.*, vol. 7, no. 8, pp. 2080–2088, Aug. 2020.

[11] Y. Yao et al., "Electrically tunable metasurface perfect absorbers for ultrathin mid-infrared optical modulators," *Nano Lett.*, vol. 14, no. 11, pp. 6526–6532, Nov. 2014.

[12] A. Y. Modi, C. A. Balanis, C. R. Birtcher, and H. N. Shaman, "New class of RCS-reduction metasurfaces based on scattering cancellation using array theory," *IEEE Trans. Antennas Propag.*, vol. 67, no. 1, pp. 298–308, Jan. 2019.

[13] P.-Y. Chen and A. Alù, "Mantle cloaking using thin patterned metasurfaces," *Phys. Rev. B, Condens. Matter*, vol. 84, no. 20, Nov. 2011, Art. no. 205110.

[14] P. Y. Chen, C. Argyropoulos, and A. Alù, "Broadening the cloaking bandwidth with non-Foster metasurfaces," *Phys. Rev. Lett.*, vol. 111, no. 23, Dec. 2013, Art. no. 233001.

[15] M. Yazdi et al., "A bianisotropic metasurface with resonant asymmetric absorption," *IEEE Trans. Antennas Propag.*, vol. 63, no. 7, pp. 3004–3015, Jul. 2015.

[16] J. F. Wang et al., "Metantenna: When metasurface meets antenna again," *IEEE Trans. Antennas Propag.*, vol. 68, no. 3, pp. 1332–1347, Mar. 2020.

[17] H.-T. Chen, A. J. Taylor, and N. Yu, "A review of metasurfaces: Physics and applications," *Rep. Prog. Phys.*, vol. 79, no. 7, Jul. 2016, Art. no. 076401.

[18] N. Shlezinger, G. C. Alexandropoulos, M. F. Imani, Y. C. Eldar, and D. R. Smith, "Dynamic metasurface antennas for 6G extreme massive MIMO communications," *IEEE Wireless Commun.*, vol. 28, no. 2, pp. 106–113, Apr. 2021.

[19] S. Maci, G. Minatti, M. Casaletti, and M. Bosiljevac, "Metasurfing: Addressing waves on impenetrable metasurfaces," *IEEE Antennas Wireless Propag. Lett.*, vol. 10, pp. 1499–1502, 2012.

[20] Y. He, Y. Li, L. Zhu, and P.-Y. Chen, "Miniaturization of omnidirectional cavity antennas using substrate-integrated impedance surfaces," *IEEE Trans. Antennas Propag.*, vol. 69, no. 3, pp. 1728–1733, Mar. 2021.

[21] Y. He and Y. Li, "Dual-polarized microstrip antennas with capacitive via fence for wide beamwidth and high isolation," *IEEE Trans. Antennas Propag.*, vol. 68, no. 7, pp. 5095–5103, Jul. 2020.

[22] Y. Jia, Y. Liu, H. Wang, K. Li, and S. Gone, "Low-RCS, high-gain, and wideband mushroom antenna," *IEEE Antennas Wireless Propag. Lett.*, vol. 14, pp. 277–280, 2015.

[23] Y. Zhao, X. Cao, J. Gao, X. Yao, and X. Liu, "A low-RCS and high-gain slot antenna using broadband metasurface," *IEEE Antennas Wireless Propag. Lett.*, vol. 15, pp. 290–293, 2016.

[24] Y. Fan, J. Wang, Y. Li, J. Zhang, Y. Han, and S. Qu, "Low-RCS and high-gain circularly polarized metasurface antenna," *IEEE Trans. Antennas Propag.*, vol. 67, no. 12, pp. 7197–7203, Dec. 2019.

[25] S. Genovesi, F. Costa, and A. Monorchio, "Low-profile array with reduced radar cross section by using hybrid frequency selective surfaces," *IEEE Trans. Antennas Propag.*, vol. 60, no. 5, pp. 2327–2335, May 2012.

[26] Y. Zheng, J. Gao, X. Cao, Z. Yuan, and H. Yang, "Wideband RCS reduction of a microstrip antenna using artificial magnetic conductor structures," *IEEE Antennas Wireless Propag. Lett.*, vol. 14, pp. 1582–1585, 2015.

[27] A. Y. Modi, C. A. Balanis, C. R. Birtcher, and H. N. Shaman, "Novel design of ultrabroadband radar cross section reduction surfaces using artificial magnetic conductors," *IEEE Trans. Antennas Propag.*, vol. 65, no. 10, pp. 5406–5417, Oct. 2017.

[28] A. Edalati and K. Sarabandi, "Wideband, wide angle, polarization independent RCS reduction using nonabsorptive miniaturized-element frequency selective surfaces," *IEEE Trans. Antennas Propag.*, vol. 62, no. 2, pp. 747–754, Sep. 2014.

[29] G. Von Trentini, "Partially reflecting sheet arrays," *IRE Trans. Antennas Propag.*, vol. 4, no. 4, pp. 666–671, Oct. 1956.

[30] A. Pirhadi, H. Bahrami, and J. Nasri, "Wideband high directive aperture coupled microstrip antenna design by using a FSS superstrate layer," *IEEE Trans. Antennas Propag.*, vol. 60, no. 4, pp. 2101–2106, Apr. 2012.

[31] A. R. Weily, T. S. Bird, and Y. J. Guo, "A reconfigurable high-gain partially reflecting surface antenna," *IEEE Trans. Antennas Propag.*, vol. 56, no. 11, pp. 3382–3390, Nov. 2008.

[32] A. P. Feresidis, G. Goussetis, S. Wang, and J. C. Vardaxoglou, "Artificial magnetic conductor surfaces and their application to low-profile high-gain planar antennas," *IEEE Trans. Antennas Propag.*, vol. 53, no. 1, pp. 209–215, Jan. 2005.

[33] Z. H. Zhou, Y. Li, Y. J. He, Z. J. Zhang, and P. Y. Chen, "A slender Fabry–Pérot antenna for high-gain horizontally polarized omnidirectional radiation," *IEEE Trans. Antennas Propag.*, vol. 69, no. 1, pp. 526–531, Jan. 2021.

[34] R. Gardelli, M. Albani, and F. Capolino, "Array thinning by using antennas in a Fabry–Pérot cavity for gain enhancement," *IEEE Trans. Antennas Propag.*, vol. 54, no. 7, pp. 1979–1990, Jul. 2006.

[35] A. Hosseini, F. Capolino, and F. De Flaviis, "Gain enhancement of a V-band antenna using a Fabry–Pérot cavity with a self-sustained all-metal cap with FSS," *IEEE Trans. Antennas Propag.*, vol. 63, no. 3, pp. 909–921, Mar. 2015.

[36] W. Pan, C. Huang, P. Chen, X. Ma, C. Hu, and X. Luo, "A low-RCS and high-gain partially reflecting surface antenna," *IEEE Trans. Antennas Propag.*, vol. 62, no. 2, pp. 945–949, Feb. 2014.

[37] H. Jiang, Z. Xue, W. Li, W. Ren, and M. Cao, "Low-RCS high-gain partially reflecting surface antenna with metamaterial ground plane," *IEEE Trans. Antennas Propag.*, vol. 64, no. 9, pp. 4127–4132, Sep. 2016.

[38] L. Zhang et al., "Realization of low scattering for a high-gain Fabry–Pérot antenna using coding metasurface," *IEEE Trans. Antennas Propag.*, vol. 65, no. 7, pp. 3374–3383, Jul. 2017.

[39] J. Y. Ren, W. Jiang, K. Z. Zhang, and S. X. Gong, "A high-gain circularly polarized Fabry–Pérot antenna with wideband low-RCS property," *IEEE Antennas Wireless Propag. Lett.*, vol. 17, no. 5, pp. 853–856, May 2018.

[40] K. Niotaki, A. Collado, A. Georgiadis, S. Kim, and M. M. Tentzeris, "Solar/electromagnetic energy harvesting and wireless power transmission," *Proc. IEEE*, vol. 102, no. 11, pp. 1712–1722, Nov. 2014.

[41] H. C. Qiu et al., "Compact, flexible, and transparent antennas based on embedded metallic mesh for wearable devices in 5G wireless network," *IEEE Trans. Antennas Propag.*, vol. 69, no. 4, pp. 1864–1873, Apr. 2021.

[42] Y. Zhang, S. Shen, C. Y. Chiu, and R. Murch, "Hybrid RF-solar energy harvesting systems utilizing transparent multiport micromeshed antennas," *IEEE Trans. Microw. Theory Techn.*, vol. 67, no. 11, pp. 4534–4546, Nov. 2019.

[43] R. B. Green et al., "Optically transparent antennas and filters: A smart city concept to alleviate infrastructure and network capacity challenges," *IEEE Antennas Propag. Mag.*, vol. 61, no. 3, pp. 37–47, Jun. 2019.

[44] R. B. Green et al., "An alternative material for transparent antennas for commercial and medical applications," *Microw. Opt. Technol. Lett.*, vol. 59, pp. 773–777, Apr. 2017.

[45] Y. Rahmat-Samii, V. Manohar, and J. M. Kovitz, "For satellites, think small, dream big: A review of recent antenna developments for CubeSats," *IEEE Antennas Propag. Mag.*, vol. 59, no. 2, pp. 22–30, Apr. 2017.

[46] X. Y. Liu et al., "Transparent and nontransparent microstrip antennas on a CubeSat: Novel low-profile antennas for CubeSats improve mission reliability," *IEEE Antennas Propag. Mag.*, vol. 59, no. 2, pp. 59–68, Apr. 2017.

[47] J. R. Saberin and C. Furse, "Challenges with optically transparent patch antennas," *IEEE Antennas Propag. Mag.*, vol. 54, no. 3, pp. 10–16, Jun. 2012.

[48] T. W. Turpin and R. Baktur, "Meshed patch antennas integrated on solar cells," *IEEE Antennas Wireless Propag. Lett.*, vol. 8, pp. 693–696, 2009.

[49] W. Hong, S. Lim, S. Ko, and Y. G. Kim, "Optically invisible antenna integrated within an OLED touch display panel for IoT applications," *IEEE Trans. Antennas Propag.*, vol. 65, no. 7, pp. 3750–3755, Jul. 2017.

[50] Y. D. Xu et al., "Pencil–paper on-skin electronics," *Proc. Nat. Acad. Sci. USA*, vol. 117, no. 31, pp. 18292–18301, Aug. 2020.

[51] L. Zhu, T. D. Ha, Y.-H. Chen, H. Huang, and P.-Y. Chen, "A passive smart face mask for wireless cough monitoring: A harmonic detection scheme with clutter rejection," *IEEE Trans. Biomed. Circuits Syst.*, vol. 16, no. 1, pp. 129–137, Feb. 2022.

[52] T. Jang, C. Zhang, H. Youn, J. Zhou, and L. J. Guo, "Semitransparent and flexible mechanically reconfigurable electrically small antennas based on tortuous metallic micromesh," *IEEE Trans. Antennas Propag.*, vol. 65, no. 1, pp. 150–158, Jan. 2017.

[53] M. Kashanianfard and K. Sarabandi, "Vehicular optically transparent UHF antenna for terrestrial communication," *IEEE Trans. Antennas Propag.*, vol. 65, no. 8, pp. 3942–3949, Aug. 2017.

[54] D. Potti et al., "A novel optically transparent UWB antenna for automotive MIMO communications," *IEEE Trans. Antennas Propag.*, vol. 69, no. 7, pp. 3821–3828, Jul. 2021.

[55] A. Desai, T. Upadhyaya, and R. Patel, "Compact wideband transparent antenna for 5G communication systems," *Microw. Opt. Technol. Lett.*, vol. 61, no. 3, pp. 781–786, Mar. 2019.

[56] A. Foroozesh and L. Shafai, "Investigation into the effects of the patch-type FSS superstrate on the high-gain cavity resonance antenna design," *IEEE Trans. Antennas Propag.*, vol. 58, no. 2, pp. 258–270, Feb. 2010.

[57] R. Orr, G. Goussetis, and V. Fusco, "Design method for circularly polarized Fabry–Pérot cavity antennas," *IEEE Trans. Antennas Propag.*, vol. 62, no. 1, pp. 19–26, Jan. 2014.

[58] N. Wang, Q. Liu, C. Wu, L. Talbi, Q. Zeng, and J. Xu, "Wideband Fabry–Pérot resonator antenna with two complementary FSS layers," *IEEE Trans. Antennas Propag.*, vol. 62, no. 5, pp. 2463–2471, May 2014.

[59] A. P. Feresidis and J. C. Vardaxoglou, "High gain planar antenna using optimised partially reflective surfaces," *IEE Proc.-Microw., Antennas Propag.*, vol. 148, no. 6, pp. 345–350, Dec. 2001.

[60] D. M. Pozar, *Microwave Engineering*, 4th ed. New York, NY, USA: Wiley, 2011, p. 192.

[61] Y. R. Padooru, A. B. Yakovlev, P.-Y. Chen, and A. Alù, "Line-source excitation of realistic conformal metasurface cloaks," *J. Appl. Phys.*, vol. 112, no. 10, Nov. 2012, Art. no. 104902.

[62] Y. R. Padooru, A. B. Yakovlev, P.-Y. Chen, and A. Alù, "Analytical modeling of conformal mantle cloaks for cylindrical objects using sub-wavelength printed and slotted arrays," *J. Appl. Phys.*, vol. 112, no. 3, Aug. 2012, Art. no. 034907.

[63] P.-Y. Chen, J. Soric, Y. R. Padooru, H. M. Bernety, A. B. Yakovlev, and A. Alù, "Nanostructured graphene metasurface for tunable terahertz cloaking," *New J. Phys.*, vol. 15, no. 12, Dec. 2013, Art. no. 123029.

[64] F. Costa, S. Genovesi, A. Monorchio, and G. Manara, "A circuit-based model for the interpretation of perfect metamaterial absorbers," *IEEE Trans. Antennas Propag.*, vol. 61, no. 3, pp. 1201–1209, Mar. 2013.

[65] F. Costa, A. Monorchio, and G. Manara, "Analysis and design of ultra thin electromagnetic absorbers comprising resistively loaded high impedance surfaces," *IEEE Trans. Antennas Propag.*, vol. 58, no. 5, pp. 1551–1558, May 2010.

[66] ANSYS. (2021). *HFSS: High Frequency Structure Simulator Based on Finite Element Method*. [Online]. Available: https://www.ansys.com/products/electronics/ansys-hfss

[67] H. Liu, V. Avrutin, N. Izyumskaya, Ü. Özgür, and H. Morkoç, "Transparent conducting oxides for electrode applications in light emitting and absorbing devices," *Superlattices Microstruct.*, vol. 48, no. 5, pp. 458–484, Nov. 2010.

[68] O. Tuna, Y. Selamet, G. Aygun, and L. Ozyuzer, "High quality ITO thin films grown by DC and RF sputtering without oxygen," *J. Phys. D, Appl. Phys.*, vol. 43, no. 5, Feb. 2010, Art. no. 055402.

[69] H. Kim et al., "Electrical, optical, and structural properties of indium–tin–oxide thin films for organic light-emitting devices," *J. Appl. Phys.*, vol. 86, no. 11, pp. 6451–6461, Dec. 1999.

[70] S. Bae et al., "Roll-to-roll production of 30-inch graphene films for transparent electrodes," *Nature Nanotechnol.*, vol. 5, no. 8, pp. 574–578, Aug. 2010.

[71] M. Layani and S. Magdassi, "Flexible transparent conductive coatings by combining self-assembly with sintering of silver nanoparticles performed at room temperature," *J. Mater. Chem.*, vol. 21, no. 39, pp. 15378–15382, 2011.

[72] C. Ji, D. Liu, C. Zhang, and L. Jay Guo, "Ultrathin-metal-film-based transparent electrodes with relative transmittance surpassing 100%," *Nature Commun.*, vol. 11, no. 1, p. 3367, Jul. 2020.

[73] L. Zhu, P.-Y. Chen, and C. Zhang, "High-performance, transparent and flexible antenna based on conductive nanocomposites," in *Proc. IEEE Int. Symp. Antennas Propag. North Amer. Radio Sci. Meeting*, Jul. 2020, pp. 1491–1492.

[74] H. Y. Wang et al., "Transparent perfect microwave absorber employing asymmetric resonance cavity," *Adv. Sci.*, vol. 6, no. 19, Oct. 2019, Art. no. 1901320.

[75] L. Zhu, X. Nie, P.-Y. Chen, and L. J. Guo, "Transparent and flexible self-dual antennas for hybrid inductive/capacitive and radiative power transfer," in *Proc. IEEE Wireless Power Transf. Conf. (WPTC)*, Jun. 2021, pp. 1–4.

[76] R. Rodriguez-Berral, C. Molero, F. Medina, and F. Mesa, "Analytical wideband model for strip/slit gratings loaded with dielectric slabs," *IEEE Trans. Microw. Theory Techn.*, vol. 60, no. 12, pp. 3908–3918, Dec. 2012.

[77] R. Rodriguez-Berral, F. Mesa, F. Medina, and M. Garcia-Vigueras, "Analytical circuit model for dipole frequency-selective surfaces," in *IEEE MTT-S Int. Microw. Symp. Dig.*, Jun. 2013, pp. 1–4.

[78] PowerFilm SOLAR Inc. (Aug. 2021). *Indoor Light Series Solar Panels—LL200-3-37*. [Online]. Available: https://www.powerfilmsolar.com/products/electronic-component-solar-panels/indoor-light-series/ll200-3-37

[79] F. Meng and S. K. Sharma, "A dual-band high-gain resonant cavity antenna with a single layer superstrate," *IEEE Trans. Antennas Propag.*, vol. 63, no. 5, pp. 2320–2325, May 2015.

[80] B. Luk'yanchuk et. al., "The Fano resonance in plasmonic nanostructures and metamaterials," *Nature Mater.*, vol. 9, pp. 707–715, Aug. 2010.

[81] M. F. Limonov, M. V. Rybin, A. N. Poddubny, and Y. S. Kivshar, "Fano resonances in photonics," *Nature Photon.*, vol. 11, no. 9, pp. 543–554, 2017.

[82] C. A. Balanis, *Antenna Theory: Analysis and Design*, 4th ed. Hoboken, NJ, USA: Wiley, 2016, pp. 83–87.

[83] B. Xi, X. Liang, Q. Chen, K. Wang, J. Geng, and R. Jin, "Optical transparent antenna array integrated with solar cell," *IEEE Antennas Wireless Propag. Lett.*, vol. 19, no. 3, pp. 457–461, Mar. 2020.

[84] S. Zarbakhsh, M. Akbari, M. Farahani, A. Ghayekhloo, T. A. Denidni, and A.-R. Sebak, "Optically transparent subarray antenna based on solar panel for CubeSat application," *IEEE Trans. Antennas Propag.*, vol. 68, no. 1, pp. 319–328, Jan. 2020.

[85] A. T. Almutawa, A. Hosseini, D. R. Jackson, and F. Capolino, "Leaky-wave analysis of wideband planar Fabry–Pérot cavity antennas formed by a thick PRS," *IEEE Trans. Antennas Propag.*, vol. 67, no. 8, pp. 5163–5175, Aug. 2019.

Trung D. Ha (Graduate Student Member, IEEE) received the B.E. degree in electrical engineering from the Hanoi University of Science and Technology (HUST), Hanoi, Vietnam, in 2014, and the M.Sc. degree in electrical engineering from the Korea Advanced Institute of Science and Technology (KAIST), Daejeon, Republic of Korea, in 2019. He is currently pursuing the Ph.D. degree in electrical and computer engineering with the University of Illinois at Chicago, Chicago, IL, USA.

His research mainly focuses on RF/microwave devices, wireless power transfer, and wireless sensor systems.

Liang Zhu (Student Member, IEEE) received the M.Sc. degree in optics from Sun Yat-sen University, Guangzhou, China, in 2015, and the Ph.D. degree in electrical and electronics engineering from the University of Illinois at Chicago, Chicago, IL, USA, in 2021.

He currently serves as an Antenna Engineer at Maxtena, Inc., Rockville, MD, USA. His research mainly focuses on RF/microwave antennas and circuits, energy harvesting platforms, and wireless sensors.

Nabeel AlSaab received the first master's degree in electrical engineering from Wayne State University, Detroit, MI, USA, in 2017, and the second master's degree in engineering systems management from St. Mary's University, San Antonio, TX, USA, in 2011. He is currently pursuing the Ph.D. degree in electrical engineering with the University of Illinois at Chicago, Chicago, IL, USA.

He is currently a Lecturer with the Department of Electrical Engineering, College of Engineering, Qassim University, Unaizah, Saudi Arabia. His extensive programming and project management skills are applied to the design of smart sensors and wireless communication.

Pai-Yen Chen (Senior Member, IEEE) received the B.S. and M.S. degrees from National Chiao Tung University, Hsinchu, Taiwan, in 2004 and 2006, respectively, and the Ph.D. degree from the University of Texas at Austin, Austin, TX, USA, in 2013.

He was a Research Staff with National Nano Device Laboratory, Taipei, Taiwan, from 2006 to 2009, a Research Scientist at Intellectual Ventures' Metamaterial Commercialization Center, Bellevue, WA, USA, from 2013 to 2014, and an Assistant Professor at Wayne State University (WSU), Detroit, MI, USA, from 2014 to 2018. He is currently an Associate Professor with the Department of Electrical and Computer Engineering, University of Illinois, Chicago (UIC), Chicago, IL, USA. He has been involved in multidisciplinary research on applied electromagnetics, RF, microwave, millimeter-wave antennas and circuits, metamaterials, metasurfaces, wireless sensors and integrated systems, as well as nanoelectromagnetism in plasmonics and nanophotonics.

Dr. Chen has received quite a few prestigious awards, including National Science Foundation (NSF) CAREER Award, IEEE Sensors Council Young Professional Award, IEEE Raj Mittra Travel Grant (RMTG) Award, SPIE Rising Researcher Award, ACES Early Career Award, PIERS Young Scientist Award, Young Scientist Awards from URSI General Assembly and URSI Commission B: Electromagnetics, IOP Measurement Science and Technology Emerging Leader, Air Force Research Laboratory Faculty Fellowship, UIC College of Engineering Faculty Research Award, WSU College of Engineering Faculty Research Excellence Award, Donald Harrington Fellowship, Taiwan Ministry of Education Study Abroad Award, United Microelectronics Corporation Scholarship, and quite a few best paper awards and travel grants from major IEEE conferences, including IEEE Antennas and Propagation Symposium (2011, 2013, 2016, and 2021), IEEE International Microwave Symposium (2015), IEEE Sensors Conference (2016), IEEE Wireless Power Transfer Conference (2021), and USNC-URSI Ernest K. Smith Student Paper Award (2012). He was a Founder and the Chair of IEEE Sensors Council Chicago Chapter (2019–2021). He currently serves as an Associate Editor of IEEE SENSORS JOURNAL, IEEE TRANSACTIONS ON ANTENNAS AND PROPAGATION, IEEE JOURNAL OF RADIO FREQUENCY IDENTIFICATION (IEEE JRFID), IEEE JOURNAL OF ELECTROMAGNETICS, and RF AND MICROWAVES IN MEDICINE AND BIOLOGY (IEEE-JERM) and the Guest Editor of several international journals including the IEEE TRANSACTIONS ON ANTENNAS AND PROPAGATION. He was a former Associate Editor of Applied Electromagnetics. He serves on the ACES Board of Directors (2021–2024).

Jay L. Guo received the B.S. degree in physics from Nankai University, Tianjin, China, in 1990, and the M.S. and Ph.D. degrees from the University of Minnesota, Minneapolis, MN, USA, in 1995 and 1997, respectively.

He is currently a Professor with the Department of Electrical Engineering and Computer Science, University of Michigan. He directs an interdisciplinary laboratory at the intersection of electrical engineering, photonics, polymer materials, and mechanical engineering. His group's research includes polymer-based photonic devices and sensor applications, organic and hybrid photovoltaics, plasmonic nanophotonics, and scalable nanomanufacturing technologies, such as roll-to-roll nanoimprinting.